Numerical Calculation Method for Brain Shift Based on Hydrostatics and Dynamic FEM

Xiaoshuai Chen, Ryosuke Shirai, Ken Masamune, Manabu Tamura, Yoshihiro Muragaki, Kazuya Sase, Teppei Tsujita, *Member, IEEE*, and Atsushi Konno, *Member, IEEE*

***Abstract*—During neurosurgery, brain deformation occurs because of gravity and leakage of the cerebrospinal fluid (CSF), which is referred to as brain shift. Brain shift is a serious problem in neuronavigation because neuronavigation relies on preoperatively taken medical images. This paper presents a brain shift estimation method based on hydrostatics and dynamic FEM, assuming that gravity and leakage of CSF are the main reasons for brain shift. The accuracy of the proposed method was verified via basic experiments conducted using elastic gelatin cubes. In addition, a 3D brain model was created using preoperative medical images of a patient and brain shift estimation simulations were performed. Their accuracy was verified by comparing the simulation results with the actual brain shift during neurosurgery. Assuming that the node in the most anterior position of the frontal lobe and the node in the highest position of the parietal lobe before the brain shift respectively remain in the most anterior position and the highest position even after the brain shift, the corresponding regions before and after the brain shift were searched and the deformations were evaluated. In this error analysis, the maximum estimation error was 4.4 mm. Furthermore, a region of 40 mm × 30 mm in the frontal lobe was chosen as the region of interest (ROI), and the surface errors in the ROI between the intraoperative MRI images and the simulated shifted brain were analyzed. The mean absolute error (MAE) between the surfaces along the z-axis (the direction of gravity) in the ROI was 3.7 mm (maximum absolute error was 8.8 mm). The proposed method was sufficiently simple for computing the brain shift in real-time. The expected contribution of this study toward improving the neuronavigational error and enhancing the safety of neurosurgery will be beneficial for hospitals, especially when the intraoperative MRI cannot be performed.**

***Index Terms*—Brain shift, dynamic FEM, neurosurgery simulation.**

I. Introduction

THE MOST common type of malignant brain tumor is glioma [1]. Unlike other brain tumors, glioma is a tumor that infiltrates normal nerve cells extensively and is difficult to remove. It has been reported that the degree of tumor removal of a glioma and the survival time of a patient are strongly related, and removing as much of the tumor as possible by surgery improves the prognosis. However, depending on the site of the tumor, there is a high risk of severe complications such as paralysis during the removal procedure.

To remove as much of the tumors as possible without inflicting severe neuropathy, image-guided neurosurgery has been introduced. Image-guided neurosurgeries complement the personal skills of the surgeon. Different kinds of image-guidance technologies are used depending on the location and type of the tumor, among which the neuronavigation system is the most commonly used. The advantage of the neuronavigation system is that the surgeon can observe the location of the tumor and the location of the operating site in the medical image in real-time. By using the navigation system that shows the location information of the tumor, important brain regions, and nerve fibers, surgeons can remove as much of the tumor as possible during surgery, without affecting the quality of life. Therefore, the neuronavigation system enables safer and more reliable neurosurgery.

During neurosurgery, the position of the whole brain shifts, and the shape and position of the remaining tumor change when the tumor is removed. Such position shifts are collectively termed as "brain shift". Brain shift reduces the credibility of the neuronavigation system because it relies on preoperative images, whereas the actual position of the tumor shifts from the one shown in the preoperative images during surgery. This results in inaccurate navigation, which may cause serious errors during the neurosurgery.

Brain shift is caused by many factors such as the position of the patient's head and tumor resection. The major factor is a change in the balance between the gravity and buoyancy forces acting on the brain. An illustration of brain shift is shown in Fig. 1. Before the craniotomy, the brain is covered entirely by the dura, and the gap between the brain and dura is filled

Manuscript received August 27, 2021; revised December 3, 2021 and March 3, 2022; accepted April 1, 2022. Date of publication April 18, 2022; date of current version May 18, 2022. This article was recommended for publication by Associate Editor D. Stoyanov and Editor P. Dario upon evaluation of the reviewers' comments. This work was supported in part by the JSPS Grant-in-Aid for Scientific Research (A) under Grant 18H04102 and Grant 15H01707; in part by the JSPS Grant-in-Aid for Early-Career Scientists under Grant 18K13720 and Grant 22K14210; in part by the JSPS Grant-in-Aid for JSPS Fellows under Grant 15J01496; in part by the JSPS Funding Program for Next Generation World-Leading Researchers under Grant LR003; in part by JKA and its Promotion Funds from KEIRIN RACE under Grant 2018M-156; and in part by the Tateisi Science and Technology Foundation under Grant 20181017. *(Corresponding author: Xiaoshuai Chen.)*

Xiaoshuai Chen is with the Faculty of Science and Technology, Hirosaki University, Hirosaki 036-8560, Japan (e-mail: chen@hirosaki-u.ac.jp).

Ryosuke Shirai and Atsushi Konno are with the Graduate School of Information Science and Technology, Hokkaido University, Sapporo 060-0814, Japan.

Ken Masamune, Manabu Tamura, and Yoshihiro Muragaki are with the Institute of Advanced Biomedical Engineering and Science, Tokyo Women's Medical University, Tokyo 162-8480, Japan.

Kazuya Sase is with the Faculty of Engineering, Tohoku Gakuin University, Sendai 980-8511, Japan.

Teppei Tsujita is with the Department of Mechanical Engineering, National Defense Academy of Japan, Yokosuka 239-8686, Japan.

Digital Object Identifier 10.1109/TMRB.2022.3168075

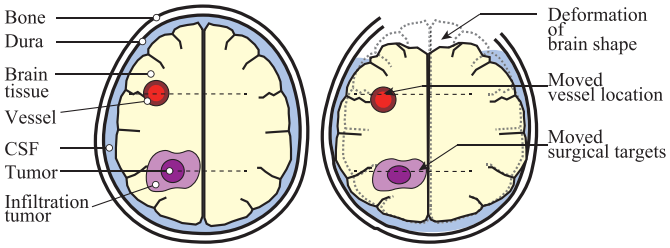

(a) Preoperative medical image taken before the surgery

(b) Intraoperative medical image taken after a craniotomy

Fig. 1. Diagram of brain shift. After a craniotomy procedure, the brain shape deforms and lesion location changes because of CSF leakage.

with cerebrospinal fluid (CSF). The densities of the brain and CSF are close; hence, the brain floats in the CSF. After the dura opening, the CSF leaks and the buoyancy force acting on the brain deceases, causing the brain to deform. It has been reported that the surface of the brain shifts by up to 20 mm and the internal brain shifts by up to 6 or 7 mm after a dura opening [2].

To account for the brain shift in neuronavigation, magnetic resonance imaging (MRI) during neurosurgery (intraoperative MRI) has been conducted in some advanced medical centers [3]. To perform the intraoperative MRI, an MRI machine must be installed in the surgery room. However, MRI machines are expensive, and the surgery room may require renovations to install an MRI machine. Therefore, only a few hospitals can perform the intraoperative MRI. Consequently, it is essential to develop a method that can accurately account for the brain shift in neuronavigation for hospitals that are not equipped with intraoperative MRI machines.

Several studies have been conducted on methods that correct the preoperative images using intraoperative information. One method involves using intraoperative ultrasound [4]. After a craniotomy, ultrasound is used to track the deformation of brain tissues and other information such as the tumor location. Using the intraoperative information, the preoperative images are readjusted to show the brain shift. However, a part of the brain becomes a blind spot owing to the arrival depth of the ultrasonic waves and the fan-shaped detection field, hampering the widespread use of this technique. Although some deformation models and functions have been developed to enhance the accuracy of the intraoperative ultrasound and preoperative image registration [5], the clinical values of intraoperative ultrasound registration for correcting brain shift still remain before dura-opening [4].

Deformation estimation is another useful method to compensate for brain shift. As mentioned above, the gravity acting on the brain tissue and the buoyancy from the liquid must be considered while compensating for brain shift. A moving particle simulation-finite element method (MPS-FEM) coupled analysis algorithm focusing on the interaction between the liquid and solid was proposed by Ema *et al.* [6]. The flow of the liquid was calculated by the MPS, whereas the deformation of the brain was treated as a linear elastic model and calculated by the FEM. Antonio *et al.* proposed a hybrid poro-hyper-viscoelastic material formulation to simulate brain shift, and they compared the simulation results with those of a brain tissue mimic [7]. Both these studies incurred a high computational cost and could not be performed in real-time. For neurosurgery, latency in navigation will significantly decrease the efficiency. Some previous studies attempted to accelerate the calculations for compensating brain shift. Sun *et al.* proposed a brain shift estimation method wherein the deformation of the whole brain was predicted by using a continuum model and FEM. The model was updated in order to minimize the error between the cortical surface intraoperatively measured by a laser range scanner (LRS) and the surface predicted by the model [8]. The two-step process, prediction and registration, is very efficient because when the deformation of brain is previously predicted, the subsequent registration will be more reliable and faster. The total update process took 11–13 min, which was not sufficiently small for real-time navigation [8]. The reduction in the computational time for prediction will significantly contribute toward improving the efficiency of total brain shift estimation process. Although the computational power of computers is increasing every day, developing a new, simple computational method for the real-time calculation of brain shift compensation remains one of the major problems while considering brain shift in neuronavigation.

After the brain shift is estimated, a surgeon proceeds to access the affected area, through a surgical hole or by opening a brain fissure. However, conventional neuronavigation systems are not equipped to process a deformation caused by the surgical operation, such as opening a brain fissure. In future, surgical navigation is expected to improve the localization of the affected area during a surgery.

Researchers have been developing a surgical navigation based on a real-time digital twin. A concept of this surgical navigation is illustrated in Fig. 2 and is explained below. During a surgery, surgeons use surgical instruments with markers that track and capture the movements of surgical instruments by a motion capture (MoCap) system. Based on the movements of instruments, dynamic simulation is performed to predict the deformation of organs and stress generated. The surfaces of organs at the surgical site are measured using a sensor, such as a laser range scanner or an RGB-D camera. The predicted deformation of an organ is corrected by the registration process using the intraoperative images or point cloud. Finally, the visuals of deformation and stress are displayed for surgeons. A measurement system of the surgical instrument movements has been reported in [9], wherein multiple surgical instruments could be tracked simultaneously. Using the measurement system, laparoscopic surgical skills in wet lab training were evaluated based on machine learning [10]. The current study is focused on the prediction of deformation based on dynamic simulation. Real-time registration for updating models will be future work.

The purpose of this study is to propose a deformation model to compensate for brain shift in real-time. The method proposed in this study has the following important advantages. First, the proposed algorithm, to realize a real-time digital twin as illustrated in Fig. 2, was simple in terms of its computational cost while ensuring accuracy. The deformation of the brain

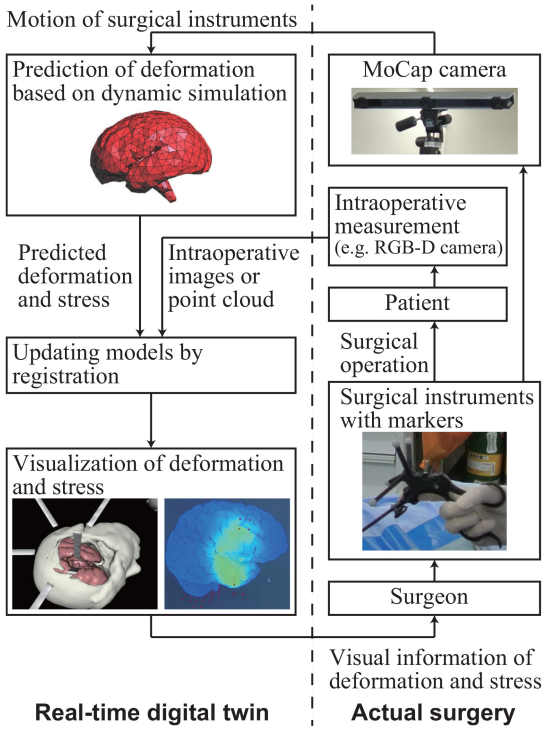

Fig. 2. A concept of a future surgical navigation.

tissue was calculated using dynamic FEM, considering gravity and the buoyancy caused by the CSF as external forces. The buoyancy was calculated using hydrostatics similar to several previous studies on brain shift compensation [11], [12]. The main improvement in the proposed method over the previously suggested methods (such as those in [11], [12]) was the use of dynamic FEM to compute the brain deformation. Although the brain shift caused by the CSF leakage is a quasi-static deformation, the proposed method can contribute to making a real-time digital twin illustrated in Fig. 2 in dynamic environments such as opening of a brain fissure or removal of a lesion. When the removal of a lesion is simulated by removing the elements of the model corresponding to the lesion, point contacts or line contacts may occur in the removed elements. In such cases, static FEM cannot be performed because the rank of the stiffness matrix is deficient, whereas dynamic FEM can be performed because the mass matrices always have a full rank even when the stiffness matrix is rank-deficient. Second, the proposed calculation method was verified using patient personal intraoperative three dimensional (3D) MRI data, whereas the previous studies used two dimensional MRI images to verify the accuracy of brain shift compensation [13], [14]. Brain shifts occur in a 3D space rather than on a two dimensional plane, so the accuracy of a brain shift estimation should be verified with respect to 3D coordinate systems. In summary, this study aims to provide a useful and uncomplicated means of brain shift compensation and to reduce the intraoperative burden on doctors.

For the initial registration between medical images (or a 3D model generated from the medical images) and patient's head, Watanabe *et al.* proposed to use three natural landmarks, the nasion and bilateral pre-auricular points, as fiducial points for registration instead of using markers [15]. In this study, we assumed that the initial registration between the medical images (or the 3D model generated from the medical images) and the patient's head can be performed by any established methods, and therefore, this paper discuss the brain shift estimations without focusing on the registration methods. Real-time intraoperative registration between the predicted deformed brain model and actual patient's head will be discussed in future works.

The overall structure of the paper consists of six sections, including this introductory section. The second section describes the proposed numerical method of brain shift estimation. The third section outlines the verification of the accuracy of proposed method using a cubic block of gelatin. The fourth section presents a brain shift simulation using a specific patient brain and focuses on the confirmation of the reproducibility of the brain shift after a craniotomy by comparing it with the data set of an intraoperative MRI. The fifth section describes the analysis of error between the surface of frontal cortex calculated through simulation and obtained from intraoperative MRI. The final section provides the conclusion of this study and the scope for future research.

II. Numerical Calculation Method of Brain Shift Estimation

A. Calculating the Brain Deformation Using FEM

The numerical calculation of the brain deformation was done by dynamic FEM. The solid brain model was divided into tetrahedral finite elements (FEs). The governing equation for the dynamic FEM is given by

$$\mathbf{F}_{external} = \mathbf{M}\ddot{\mathbf{U}} + \mathbf{C}\dot{\mathbf{U}} + \mathbf{K}\mathbf{U}, \tag{1}$$

where $\mathbf{F}_{external}$ is the external force vector; $\ddot{\mathbf{U}}$, $\dot{\mathbf{U}}$, and $\mathbf{U}$ are the acceleration, velocity, and displacement vectors of the nodes, respectively, and $\mathbf{M}$, $\mathbf{C}$, and $\mathbf{K}$ are the mass, damping, and stiffness matrices, respectively.

In the inertial term, the mass matrix is expressed using the lumped mass method. The mass matrix is calculated by

$$\mathbf{M} = \text{blockdiag}[m_1\mathbf{I}_3,\ m_2\mathbf{I}_3, \ldots, m_i\mathbf{I}_3, \ldots, m_N\mathbf{I}_3], \tag{2}$$

where N is the number of nodes and $\mathbf{I}_3$ is a 3×3 identity matrix. The mass of a tetrahedral element is assumed to be equally divided and attached to the four nodes of the element. When the mass of element k is expressed by $mass_k$, and node i is shared by $N_{element}$ elements, the nodal mass m_i is calculated as

$$m_i = \sum_{k}^{N_{element}} \frac{mass_k}{4}. \tag{3}$$

The mass of an element was calculated using the density of the brain and the volume of the element.

The damping matrix was expressed by assuming Rayleigh damping. The formula of the Rayleigh damping matrix is given by

$$\mathbf{C} = \alpha\mathbf{M} + \beta\mathbf{K}, \tag{4}$$

where α and β are the Rayleigh damping coefficients.

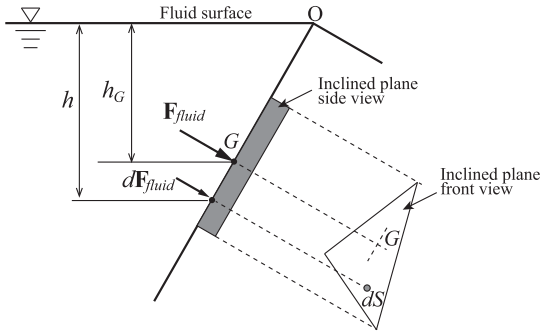

Fig. 3. The hydrostatic force acting on the plane immersed in the fluid.

The stiffness matrix was constructed using first-order tetrahedral elements.

$\mathbf{U}$, $\dot{\mathbf{U}}$, and $\ddot{\mathbf{U}}$ were calculated by applying the Newmark average constant acceleration method, which is an unconditionally stable time integration, to (1). The conjugate gradient method was adopted to obtain an approximate solution of the matrix inversion instead of calculating it directly to save calculation time.

$\mathbf{F}_{external}$ includes the gravitational force $\mathbf{F}_{gravity}$ and buoyancy force $\mathbf{F}_{fluid}$ generated by the hydraulic pressure. Ideally, $\mathbf{F}_{external}$ should also include forces from the instruments and other organs such as bones, but these forces were not considered in this study. $\mathbf{F}_{external}$ is written as

$$\mathbf{F}_{external} = \mathbf{F}_{gravity} + \mathbf{F}_{fluid}. \tag{5}$$

The gravity acts on the nodes along the negative direction of the z-axis of the world coordinate system. $\mathbf{F}_{gravity}$ is given by

$$\mathbf{F}_{gravity} = \left[[0\ 0\ m_1 g], \quad [0\ 0\ m_2 g], \quad \ldots, \quad [0\ 0\ m_N g]\right]^T, \tag{6}$$

where $g (g < 0)$ is the gravity acceleration.

In the static FEM, $\mathbf{F} = \mathbf{KU}$, the displacement vector $\mathbf{U}$ cannot be obtained when the stiffness matrix $\mathbf{K}$ is rank-deficient. However, in the dynamic FEM, it is evident from (1) that $\mathbf{U}$ can be calculated by integrating $\ddot{\mathbf{U}}$ even when the stiffness matrix $\mathbf{K}$ is rank-deficient, because the mass matrix $\mathbf{M}$ has a full rank, as described in Section I. The rank-deficiency of the stiffness matrix frequently occurs in the simulation of dissection and removal of a lesion.

B. Calculating the Force Applied by Fluid Using Hydrostatics

In this study, the CSF was assumed to be a homogeneous and an incompressible fluid. Hydrostatics was used to calculate the force applied by the fluid on the brain.

The basic concept of the hydrodynamic buoyancy calculation is shown in Fig. 3. An inclined flat plane immersed in fluid was considered, whose surface area is denoted by S. dS denotes a small part of the area S and h denotes the depth of dS below the fluid surface. With a fluid density of ρ_{fluid}, the pressure at depth h is calculated as $\rho_{fluid} g h$, and static buoyancy acting on the area dS is given by

$$\mathrm{d}F_{fluid} = \rho_{fluid} g h \mathrm{d}S. \tag{7}$$

The total force F_{fluid} on the area S is the summation of all the dF_{fluid} as follows.

$$\begin{aligned} F_{fluid} &= \int_S \rho_{fluid} g h \mathrm{d}S \\ &= \rho_{fluid} g \int_S h \mathrm{d}S \\ &= \rho_{fluid} g h_G S, \end{aligned} \tag{8}$$

where h_G is the depth of the centroid of the area S. Equation (8) shows that the total force of the fluid on a plane area is equal to the product of the area and the pressure at its centroid.

According to the theory of hydrostatics, the buoyancy vector is always normal to the object surface. Denoting the unit normal vector of the plane surface with $\mathbf{n}$, the buoyancy vector acting on the plane is calculated as

$$\mathbf{F}_{fluid} = -F_{fluid}\mathbf{n}. \tag{9}$$

The theory of hydrostatics was extended to calculate the buoyancy exerted on a solid finite element (FE) model. As shown in Fig. 4 (a), it is assumed that a part of the solid FE model is immersed in the fluid. The model was divided into linear tetrahedron elements, whose triangular surface meshes were detected beforehand and subjected to the fluid force.

A triangular surface mesh k has three vertices which are referred to as nodes in FE models. The position vector of a node i of the mesh k is denoted by $\mathbf{j}_{ki} = \left[j_{kix} \ \ j_{kiy} \ \ j_{kiz}\right]^T$ $(i = 1, 2, 3)$. Let $z = h_{fluid}$ be the z-coordinate of the fluid surface. Depending on the relationship between j_{kiz} and h_{fluid}, the position of the surface mesh k was divided into four cases: (case 1) all three nodes are under the fluid, (case 2) two nodes are under the fluid and one node is in the air, (case 3) one node is under the fluid and two nodes are in the air, and (case 4) all three nodes are in the air. The fluid force in each of the cases is calculated as follows.

Case 1: All three nodes are under the fluid surface.

If $j_{k1z},\ j_{k2z},\ j_{k3z} \le h_{fluid}$, the triangle Δk is immersed in the fluid (see Fig. 4 (b)). The centroid $\mathbf{G}_k$ of the surface mesh k is given by

$$\mathbf{G}_k\left(G_{kx}, G_{ky}, G_{kz}\right) = \frac{1}{3}\left(\mathbf{j}_{k1} + \mathbf{j}_{k2} + \mathbf{j}_{k3}\right). \tag{10}$$

The total fluid force acting on the mesh is given by

$$\mathbf{F}_{fluid(\Delta k)} = -\rho_{fluid} g (h_{fluid} - G_{kz}) S_{\Delta k} \mathbf{n}_k, \tag{11}$$

where $S_{\Delta k}$ is the area of the mesh and $\mathbf{n}_k$ is the unit normal vector of the mesh.

In general, FE analysis assumes that external force is applied to the nodes. Therefore, the force $\mathbf{F}_{fluid}(\Delta k)$ is transformed into the force $\mathbf{F}_{ki}$ applied to a node i of the mesh k. The weight distribution depends on the node depth. The node depth is given by

$$h_{ki} = h_{fluid} - j_{kiz} \quad (i = 1, 2, 3). \tag{12}$$

The nodal force at node i of mesh k is

$$\mathbf{F}_{ki} = \frac{h_{ki}}{h_{k1} + h_{k2} + h_{k3}} \mathbf{F}_{fluid(\Delta k)} \quad (i = 1, 2, 3). \tag{13}$$

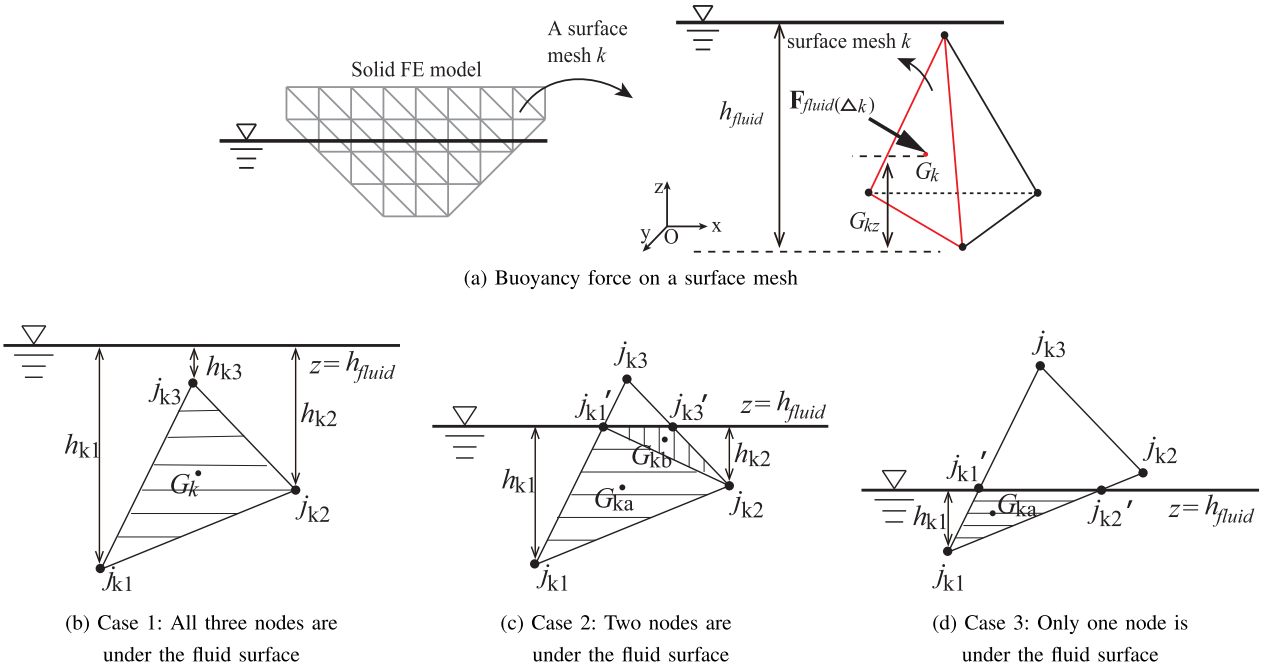

(a) Buoyancy force on a surface mesh

(b) Case 1: All three nodes are under the fluid surface

(c) Case 2: Two nodes are under the fluid surface

(d) Case 3: Only one node is under the fluid surface

Fig. 4. Buoyancy force on a surface mesh of a finite element model calculated in different cases.

Case 2: Two nodes are under the fluid and one node is in the air.

If $j_{k1z},\ j_{k2z} \leq h_{fluid}$ and $j_{k3z} > h_{fluid}$, the triangle Δk is partly immersed in the fluid (see Fig. 4 (c)). The points at the intersection of the fluid surface $z = h_{fluid}$ are denoted by j_1' and j_3'. The immersed part was divided into two triangles, $\Delta j_1 j_2 j_1'$ and $\Delta j_2 j_3' j_1'$. Let $\mathbf{G}_{ka}$ and $\mathbf{G}_{kb}$ be the centroids and $\mathbf{n}_{ka}$ and $\mathbf{n}_{kb}$ be the unit normal vectors of the triangles $\Delta j_1 j_2 j_1'$ and $\Delta j_2 j_3' j_1'$, respectively. Similar to *Case 1*, the fluid forces acting on the $S_{\Delta j_1 j_2 j_1'}$ and $S_{\Delta j_2 j_3' j_1'}$ are given by

$$\mathbf{F}_{fluid(\Delta j_1 j_2 j_1')} = -\rho_{fluid} g\left(h_{fluid} - G_{kaz}\right) S_{\Delta j_1 j_2 j_1'} \mathbf{n}_{ka}, \quad (14)$$

$$\mathbf{F}_{fluid(\Delta j_2 j_3' j_1')} = -\rho_{fluid} g\left(h_{fluid} - G_{kbz}\right) S_{\Delta j_2 j_3' j_1'} \mathbf{n}_{kb}. \quad (15)$$

$\mathbf{F}_{fluid(\Delta j_1 j_2 j_1')}$ and $\mathbf{F}_{fluid(\Delta j_2 j_3' j_1')}$ are distributed among the nodes j_{k1} and j_{k2}. Considering the weight, the nodal forces are given by

$$\mathbf{F}_{j_1} = \frac{h_1}{h_1 + h_2} \mathbf{F}_{fluid(\Delta j_1 j_2 j_1')}, \quad (16)$$

$$\mathbf{F}_{j_2} = \frac{h_2}{h_1 + h_2} \mathbf{F}_{fluid(\Delta j_1 j_2 j_1')} + \mathbf{F}_{fluid(\Delta j_2 j_3' j_1')}. \quad (17)$$

Case 3: One node is under the fluid and two nodes are in the air.

If $j_{k1z} \leq h_{fluid}$ and $j_{k2z},\ j_{k3z} > h_{fluid}$, the triangle Δk is partly immersed in the fluid (see Fig. 4 (d)). The points at the intersection of the fluid surface $z = h_{fluid}$ are denoted by j_1' and j_2'. Similar to the $\Delta j_2 j_3' j_1'$ of *Case 2*, the total fluid force acting on the $S_{\Delta j_1 j_2' j_1'}$ is

$$\mathbf{F}_{fluid(\Delta j_1 j_2' j_1')} = -\rho_{fluid} g\left(h_{fluid} - G_{kaz}\right) S_{\Delta j_1 j_2' j_1'} \mathbf{n}_{ka}. \quad (18)$$

$\mathbf{F}_{fluid(\Delta j_1 j_2' j_1')}$ is entirely transferred to node j_1, therefore the nodal force at node j_1 is

$$\mathbf{F}_{j_1} = \mathbf{F}_{fluid(\Delta j_1 j_2' j_1')}. \quad (19)$$

Case 4: All three nodes are in the air.

If $j_{k1z},\ j_{k2z},\ j_{k3z} > h_{fluid}$, the triangle Δk is not immersed in the fluid and the fluid force is $\mathbf{0}$. There is no fluid force to be distributed among the three nodes of the mesh.

The fluid force acting on a node j_{ki} is the sum of the $\mathbf{F}_{j_{ki}}$ of all the meshes that share the node j. When node j is shared by N_{mesh} meshes, the nodal fluid force $\mathbf{F}_{fluid_{j_i}}$ is given by

$$\mathbf{F}_{fluid_j} = \sum_{k}^{N_{mesh}} \mathbf{F}_{j_{ki}}. \quad (20)$$

Therefore, $\mathbf{F}_{fluid}$ in (5) is calculated by

$$\mathbf{F}_{fluid} = \begin{bmatrix} \mathbf{F}_{fluid_1} & \mathbf{F}_{fluid_2} & \cdots & \mathbf{F}_{fluid_N} \end{bmatrix}^T. \quad (21)$$

III. Experimental Verification Using Gelatin Cubes

A. Experimentation

Experiments were conducted to verify the accuracy of the proposed buoyancy estimation method. In the verification experiments, cubes made of water and gelatin (Wako Pure Chemical Industries, Ltd., Gelatin 077-03155) were used as substitutes for brain tissue because the mixture of gelatin and water has similar material characteristics as those of brain tissue [16]. Silicone oil (Shin-Etsu Chemical Co., Ltd., KF-99) was substituted for CSF because their densities are similar. Moreover, silicone oil is water-repellent and will not dissolve the water-soluble gelatin.

The weight ratio of gelatin to water in the cube was 3.5%. The gelatin cube of 50 mm × 50 mm × 25 mm was placed in an empty container, with a bottom surface area of 90 mm × 90 mm. As the gelatin cube was adhesive, the bottom surface of the gelatin cube was fixed to the container. The silicone oil was then poured into the container, as shown in

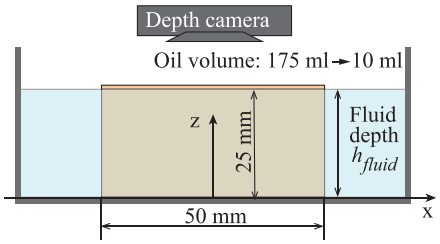

Fig. 5. Illustrations of verification experiments.

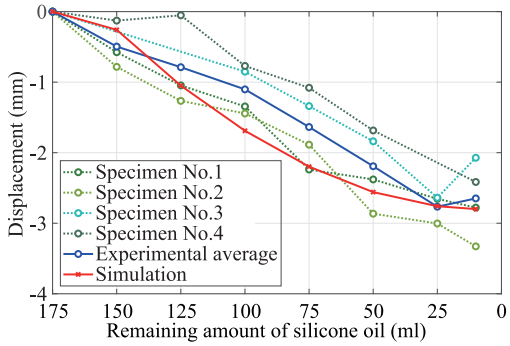

Fig. 6. Verification experiment data of the four specimens and the simulation result.

Fig. 5. The initial volume of the silicone oil was 175 ml. The upper surface of the gelatin cube was slightly above the surface of the silicon oil in the initial stage of the experiment and remained above the surface of the silicon oil during the experiments. To mimic the CSF leakage, the silicone oil volume was reduced to 150, 125, 100, 75, 50, 25, and 10 ml.

The displacement of the upper surface of the cube was measured by an RGB-D camera (Intel RealSense F200). The RGB-D camera, F200, detects the distance to an object by random pattern projection and stereo matching of the infrared (IR) cameras. However, the block of gelatin is translucent; hence, the camera could not accurately detect the distance to the upper surface of the block of gelatin. Therefore, a piece of paper was placed on the upper surface of the block so that the camera could accurately obtain the point cloud of the surface of the block. The weight of the paper was negligible. The point cloud data of the upper surface were obtained using the RGB-D camera and the displacement of the surface was calculated by taking the average of the z-coordinates of the point cloud data.

The experiment was conducted four times. The experimental results and their average were plotted in Fig. 6. The displacements at 150 and 125 ml of specimen No. 3, and at 25 ml of specimen No. 4 were not measured successfully.

B. Validation Simulation

To verify the proposed estimation method for the soft body deformation caused by a loss of equilibrium between the gravity and buoyancy forces, simulations were performed on the same scenario as of the experiments. The parameters and material properties used in the verification simulation are listed in Table I.

The Young's modulus of the gelatin cube was measured by a compression test. A uniform displacement was given to the upper surface of the cube using a table-top force tester (Shimadzu Corporation, EZ-SX). The compression was quasi-static (velocity: 0.2 mm/min) and the final displacement was 1 mm. The upper surface area of the cube was 60 mm × 60 mm. The height of the cube in the compression direction was 25 mm. The force measured by the force tester and the upper surface area were used to calculate the stress. The displacement and the initial height of the cube in the compression direction were used to calculate the strain. The Young's modulus was found to be non-linear and that it softens over time at room temperature, and it was calculated in the strain range 0.00–0.02 using a linear approximation.

TABLE I
PARAMETERS AND MATERIAL PROPERTIES USED IN THE ACCURACY VERIFICATION SIMULATION

Number of nodes	8,788
Number of elements	37,500
Silicone oil density	975 kg/m^3
Gelatin density	1,048 kg/m^3
Gelatin Young's modulus	729.1 Pa
Gelatin Poisson's ratio	0.48
Sampling time	0.05 s
Rayleigh damping coefficients	$\alpha = 0.02$, $\beta = 0.02$

The Poisson's ratio of gelatin with 4% concentration has been reported as 0.37–0.49 [17]. In the verification experiments, the gelatin was at 3.5% concentration, and the Poisson's ratio was set to 0.48 in the simulation. The densities of the gelatin cube and the silicon oil were measured as 1048 kg/m^3 and 975 kg/m^3, respectively.

The displacements of the upper surface of the cube in the simulation were plotted as shown in Fig. 6. As shown in Fig. 6, the displacement of the upper surface of the cube increases as the fluid depth decreases. The simulation results are shown to be approximately within the acceptable range of the experimental data. Therefore, the proposed method can simulate the deformation caused by the buoyancy change accurately.

C. Influence of the Numbers of Nodes and Elements of the Model

To understand the effect of the fineness of the model on the accuracy, cubic models with different numbers of nodes of 2,890, 4,851, 8,788, and 15,376 were used in simulations. The corresponding numbers of elements were 11,520, 20,000, 37,500, and 67,500. The other parameters were the ones listed in Table I. The simulation results were plotted in Fig. 7, along with the average of four experiments with error bars (from minimum to maximum). Generally, the greater the number of elements, the higher is the accuracy of the calculation. However, as shown in Fig. 7, although the number of elements increases to six times the original number, the calculation results do not show significant difference. This implies that the influence of the fineness of the model on the accuracy was not significant. This characteristic of the proposed method is very useful for the neurosurgery simulations which require real-time calculations. The balance between the number of nodes and the computational time can be decided based on the required level of accuracy and computer performance.

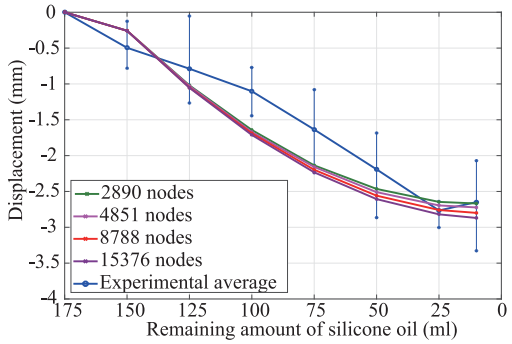

Fig. 7. Validation simulation results for different numbers of nodes and elements of the model.

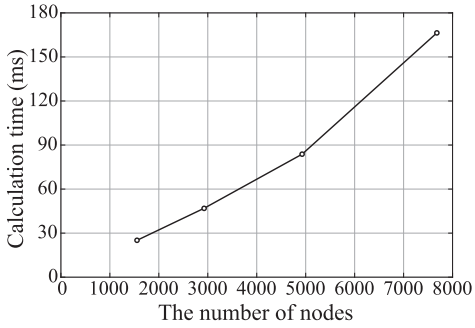

Fig. 8. Computational cost for number of nodes.

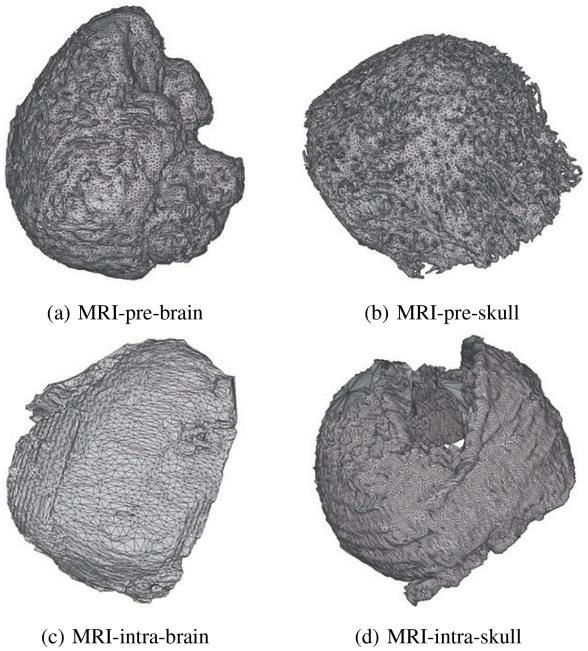

Fig. 9. Preoperative and intraoperative 3D models generated from preoperative and intraoperative MRI data. MRI-pre-brain: Preoperative brain tissue model, MRI-pre-skull: Preoperative skull model, MRI-intra-brain: Intraoperative brain tissue model, MRI-intra-skull: Intraoperative skull model.

D. Computational Cost for the Number of Nodes

The workstation KRONOS S810R (CIARA Inc., Intel Core i7 3960X, 6 cores, 3.3 [GHz]) was used to compute the numerical simulations. As mentioned in Section II-A, the conjugate gradient (CG) method was used instead of matrix inversion and was implemented on a GPU (NVIDIA R Quadro 4000, 256 CUDA cores). The mean computational times of simulation loops for various number of nodes are plotted in Fig. 8.

The computational cost of a matrix inversion is $O(n^3)$; however, as the CG method was used instead of matrix inversion, the computational time was almost linear ($O(n)$) for the number of nodes n.

IV. Verification of Brain Shift Estimation Using the Intraoperative MRI Data of an Actual Surgery

In Section III, the accuracy of the proposed deformation estimation method of a soft object immersed in fluid was verified using a simple cube model. In this section, a brain model was generated from the MRI images of an actual patient, and the brain shift was estimated by simulating the scenario of an actual neurosurgery. The accuracy was verified by comparing the simulation results and the intraoperative MRI images taken during the neurosurgery.

A. FE Model Generated From the Medical Images of a Patient

The preoperative MRI data were obtained before the neurosurgery, and the intraoperative MRI data were obtained after the craniotomy.

A free and open-source platform *3D Slicer 4.8.1* [18] was used to generate a 3D geometric model from the MRI data. The 3D Slicer can provide 3D visualization, segmentation, registration, and other functions using medical imaging data such as from MRI and computerized tomography (CT) scans. After loading the MRI data into the 3D Slicer, the *Volumes* module was first used to get a 3D model including all the parts of the patient head such as the brain and skull. Then the *Segmentation* module was used to separate the entire data into brain and skull data. Subsequently, the intraoperative MRI data were put into the 3D Slicer. The position and attitude of the patient during the intraoperative MRI were subtly different from those during the preoperative MRI. Therefore, approximate alignment was done; however, further accurate registration was needed.

For the accurate registration between the preoperative and intraoperative images from MRI, *automatic image registration* was used, which is a function of the *Registration* module of the 3D Slicer. There are three methods of automatic image registration: Elastix, ANTs, and BRAINS. Among the three methods, BRAINS were chosen, which is an intensity-based registration method named BRAINSFit [19] for whole-brain 3D images.

After this processing, rough models that had isolated parts and holes were obtained. A free and open-source mesh processing software *MeshLab 2016.12* [20] was used to repair these rough models. After repairing, four 3D models (the preoperative and intraoperative brain and skull models) as shown in Fig. 9 were obtained. The brain tissue models generated from the preoperative and intraoperative MRI data are abbreviated as “MRI-pre-brain” and “MRI-intra-brain”, respectively. Similarly, the skull models generated from the

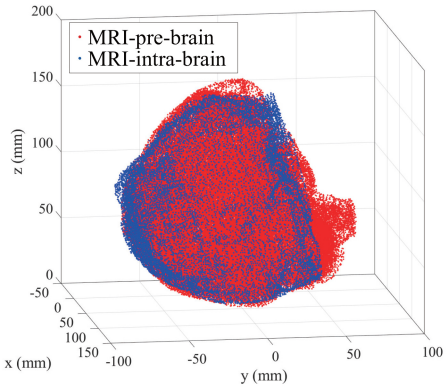

Fig. 10. Preoperative brain (red) and intraoperative brain (blue) models.

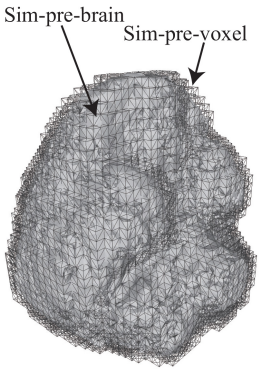

Fig. 11. Voxel meshes and surface meshes.

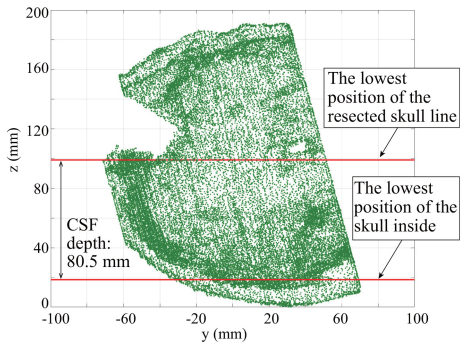

Fig. 12. The final fluid depth decision based on the intraoperative skull.

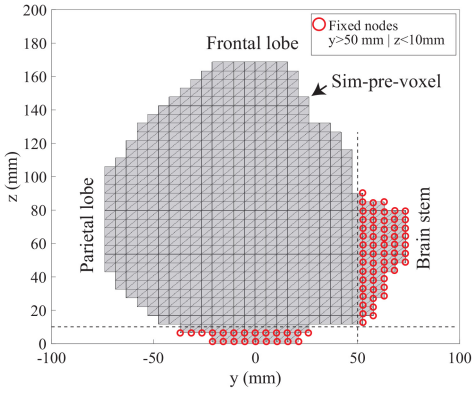

Fig. 13. Voxel model and fixed nodes.

preoperative and intraoperative MRI data are abbreviated as "MRI-pre-skull" and "MRI-intra-skull", respectively. As observed in Fig. 10, which shows the MRI-intra-brain superimposed on the MRI-pre-brain, the brain is deformed after the craniotomy because of the CSF leakage.

As shown in Fig. 9, although the 3D models generated from the medical images were repaired using MeshLab, there remain many holes and discontinuous parts in the models. Such deficient models are very difficult to divide into finite elements. It is impossible to automatically divide the models into finite elements without further sophisticated processing, which requires enormous amounts of time and effort even from professionals. To solve this problem, the *embedding* method [21] was incorporated.

Using the embedding method, the 3D geometric model was first embedded in a bounding box, whose dimensions were determined so that the box covers the 3D model entirely. Next, the bounding box was divided into voxel elements. The elements that did not include a part of the 3D model (vacant elements) were then removed. The isolated or floating elements were also removed. Finally, the voxel elements were divided into tetrahedral elements, and this tetrahedral element model was used in the finite element analysis (FEA) (see Fig. 11). The calculation cost of the FEA increases as the number of elements increases. The main advantage of the embedding method is that it makes re-meshing easy and allows it to be done online regardless of the inconsistency and incompleteness of the geometric model. Users can decide the size of the elements depending on the accuracy requirement and the computer performance.

The MRI-pre-brain was processed by the embedding method. The FE model generated from the MRI-pre-brain is abbreviated as "Sim-pre-voxel".

B. Brain Shift Simulation

A brain shift simulation was performed using the Sim-pre-voxel. The size of a voxel mesh of the FE model was 5 (mm) × 5 (mm) × 5 (mm), which was determined considering the computational cost and accuracy. The deformed FE model is referred to as "Sim-intra-voxel". The final shape of the 3D model is referred to as "Sim-intra-brain", which is transformed from the MRI-pre-brain. The position of each node in the Sim-intra-brain is calculated by linearly interpolating the displacement of the neighboring nodes in the Sim-intra-voxel.

The depth of the CSF when the preoperative MRI was taken was estimated by the highest and lowest position of the inner side of the MRI-pre-skull on the z-axis. The depth of the CSF when the intraoperative MRI was taken was estimated by the lowest position of the resected skull line and the lowest position of the inside of the skull as shown in Fig. 12. In the simulation, the CSF depth was gradually decreased till it reached the final depth and then maintained constant. For the simulation, it was assumed that the patient lay on the bed face up. Figure 13 shows the side view of the Sim-pre-brain of the

TABLE II
PARAMETERS AND MATERIAL PROPERTIES USED IN THE BRAIN SHIFT SIMULATION

Number of nodes	6,465
Number of elements	3,469
CSF density	1,000 kg/m^3
Brain density	1,036 kg/m^3
Brain Young's modulus	7.07 kPa
Brain Poisson's ratio	0.4925
Sampling time	0.2 s
Rayleigh damping coefficients	$a = 0.02$, $b = 0.02$

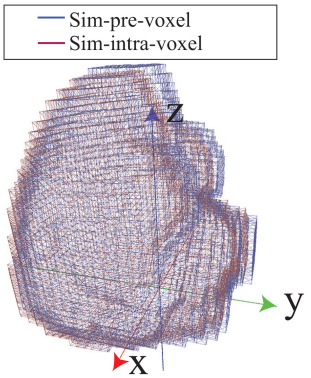

Fig. 14. The simulated brain shift.

patient. As the patient lay face up, the occipital lobe was supported by the skull through arachnoid and dura mater; hence, it was considered to be fixed in the simulation. Moreover, the brain stem was also considered to be fixed. Therefore, the nodes with $z < 10$ mm or $y > 50$ mm, which are circled in red in Fig. 13, were set as the fixed nodes.

Material properties of the brain parenchyma and CSF used in the simulation were set by referring to previous studies. The density of the CSF was set to 1000 (kg/m^3) [22]. The density and Poisson's ratio of the brain tissue were set to 1036 (kg/m^3) and 0.4925, respectively [23]. It has been reported that the shear stiffness of a whole healthy brain is $G = 2.37 \pm 0.44$ (kPa) [24]. The average value of $G = 2.37$ (kPa) was adopted and the Young's modulus E was calculated as $E = 2G(1 + \nu) = 7.07$ (kPa).

The conditions and mechanical properties used in the simulation are listed in Table II. Figure 14 shows the simulation results before the brain shift (Sim-pre-voxel) and after the brain shift (Sim-intra-voxel) of the FE model. As shown in Fig. 14, the brain deforms especially along z-axis (direction of gravity) because of the CSF leakage.

C. Accuracy Verification Using Intraoperative Medical Images

The simulation results were compared with the MRI-intra-brain to verify the simulation accuracy. The node in the most anterior position of the frontal lobe (top node in the z-coordinates), herein referred to as "node $A^{\text{MRI-pre}}$," and the node in the highest position of the parietal lobe (lowest node in the y-coordinates), herein referred to as "node $B^{\text{MRI-pre}}$," of the MRI-pre-brain (see Fig. 15) were tracked for the accuracy verification. The nodes of the Sim-pre-voxel that were

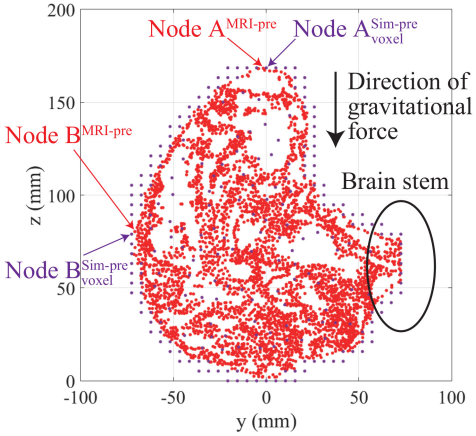

Fig. 15. The nodes A and B for accuracy verification.

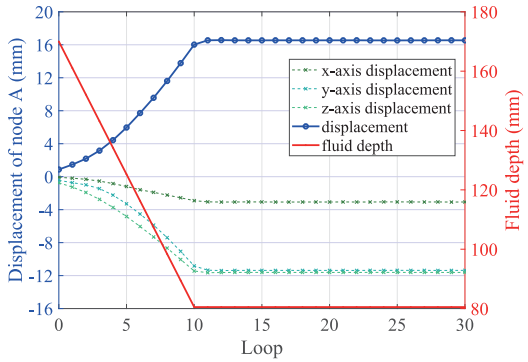

Fig. 16. The displacement of the node $A^{\text{Sim-intra}}_{\text{voxel}}$.

the closest to the nodes $A^{\text{MRI-pre}}$ and $B^{\text{MRI-pre}}$ were chosen and herein referred to as "node $A^{\text{Sim-pre}}_{\text{voxel}}$," and "node $B^{\text{Sim-pre}}_{\text{voxel}}$," respectively, as shown in Fig. 15. The displacement of the node $A^{\text{Sim-intra}}_{\text{voxel}}$ and the fluid depth in the simulation are shown in Fig. 16. The final convergent value of the displacement was compared with the intraoperative MRI data.

To examine the displacement from the pre-brain to intra-brain, it is necessary to locate the nodes corresponding to the nodes $A^{\text{MRI-pre}}$ and $B^{\text{MRI-pre}}$ in the MRI-intra-brain. However, as the surface mesh models for the MRI-pre-brain and MRI-intra-brain were created from the imaging data obtained from different MRI scans, there are no nodes in the MRI-intra-brain that correspond exactly to nodes $A^{\text{MRI-pre}}$ and $B^{\text{MRI-pre}}$. In order to locate the nodes corresponding to $A^{\text{MRI-intra}}$ and $B^{\text{MRI-intra}}$ in the intra-brain, we make the following assumptions.

1) There is no significant error between the actual brain displacement and simulation results. Therefore, the nodes $A^{\text{MRI-intra}}$ and $B^{\text{MRI-intra}}$ are in the neighborhood of $A^{\text{Sim-intra}}_{\text{voxel}}$ and $B^{\text{Sim-intra}}_{\text{voxel}}$, respectively.
2) The node in the most anterior position of the frontal lobe and the node in the highest position of the parietal lobe before the brain shift will remain in their respective positions even after the brain shift.

A concept for locating the node $A^{\text{MRI-intra}}$ is illustrated in Fig. 17. After removing the surface node outliers, an appropriate node matching the node $A^{\text{MRI-intra}}$ is searched, based on

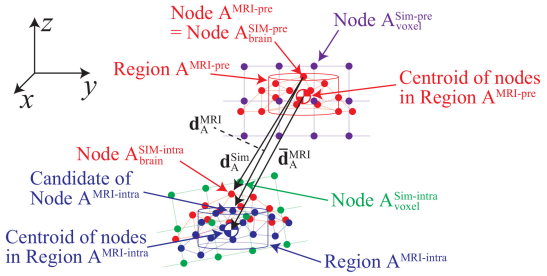

Fig. 17. Concept of finding the node $A^{\text{MRI-intra}}$.

the above assumptions, from the most anterior position (highest in the z-coordinates) near the node $A^{\text{Sim-intra}}_{\text{voxel}}$. Similarly, an appropriate node matching the node $B^{\text{MRI-intra}}$ is searched from the highest position (lowest in the y-coordinates) near the node $B^{\text{Sim-intra}}_{\text{voxel}}$.

Let $\mathbf{p}_{\text{X}}^{\text{MRI-pre}}$, $\mathbf{p}_{\text{X}}^{\text{MRI-intra}}$, and $\mathbf{p}_{\text{X,brain}}^{\text{Sim-intra}}$ be the position vectors of the nodes $X^{\text{MRI-pre}}$, $X^{\text{MRI-intra}}$, and $X^{\text{Sim-intra}}_{\text{brain}}$, respectively, where X = A or B. Note that the node $X^{\text{Sim-pre}}_{\text{brain}}$ is same as the node $X^{\text{MRI-pre}}$, hence $\mathbf{p}_{\text{X,brain}}^{\text{Sim-pre}}$ is equal to $\mathbf{p}_{\text{X}}^{\text{MRI-pre}}$.

Aforementioned, there are no nodes in the MRI-intra-brain that exactly correspond to the nodes $A^{\text{MRI-pre}}$ and $B^{\text{MRI-pre}}$. Therefore, regions were defined around the nodes $A^{\text{MRI-}j}$ and $B^{\text{MRI-}j}$ (j = pre or intra) as follows:

Region $A^{\text{MRI-}j}$:

$$\sqrt{\left(x - x_{\text{A}}^{\text{MRI-}j}\right)^2 + \left(y - y_{\text{A}}^{\text{MRI-}j}\right)^2} < 5 \text{ (mm)}$$
$$\text{and } z_{\text{A}}^{\text{MRI-}j} \geq z \geq z_{\text{A}}^{\text{MRI-}j} - 5 \text{ (mm)}$$

Region $B^{\text{MRI-}j}$:

$$\sqrt{\left(x - x_{\text{B}}^{\text{MRI-}j}\right)^2 + \left(z - z_{\text{B}}^{\text{MRI-}j}\right)^2} < 5 \text{ (mm)}$$
$$\text{and } y_{\text{B}}^{\text{MRI-}j} + 5 \geq y \geq y_{\text{B}}^{\text{MRI-}j} \text{(mm)}$$

Herein, $i_{\text{X}}^{\text{MRI-}j}$ is the i-component of $\mathbf{p}_{\text{X}}^{\text{MRI-}j}$ ($i = x$, y, or z, X = A or B, j = pre or intra). The centroid $\bar{\mathbf{p}}_{\text{X}}^{\text{MRI-}j}$ of the nodes that are included in region X is calculated. By considering the centroid of the nodes around the point of interest, the effect of registration error is expected to reduce.

The displacements of nodes for the accuracy verification are defined as follows:

$$\mathbf{d}_{\text{X}}^{\text{MRI}} = \mathbf{p}_{\text{X}}^{\text{MRI-intra}} - \mathbf{p}_{\text{X}}^{\text{MRI-pre}}, \quad (22)$$
$$\bar{\mathbf{d}}_{\text{X}}^{\text{MRI}} = \bar{\mathbf{p}}_{\text{X}}^{\text{MRI-intra}} - \bar{\mathbf{p}}_{\text{X}}^{\text{MRI-pre}}, \quad (23)$$
$$\mathbf{d}_{\text{X}}^{\text{Sim}} = \mathbf{p}_{\text{X,brain}}^{\text{Sim-intra}} - \mathbf{p}_{\text{X}}^{\text{MRI-pre}}. \quad (\text{X} = \text{A, or B}) \quad (24)$$

The error (%) of the simulated brain shift is defined as

$$\text{Error}_{X,i}(\%) = \left| \frac{d_{\text{X},i}^{\text{MRI}} - d_{\text{X},i}^{\text{sim}}}{d_{\text{X},i}^{\text{MRI}}} \right| \quad (\text{X = A or B}, i = x, y, z). \quad (25)$$

The simulated brain shifts at the nodes A and B, i.e., $\mathbf{d}_{\text{X}}^{\text{Sim}}$, are compared with both $\mathbf{d}_{\text{X}}^{\text{MRI}}$ and $\bar{\mathbf{d}}_{\text{X}}^{\text{MRI}}$. The results are presented in Table III.

TABLE III
THE ACCURACY VERIFICATION OF THE DISPLACEMENTS OF THE NODES A AND B

Node A	x-axis	y-axis	z-axis	Norm
$\mathbf{d}_{\text{A}}^{\text{MRI}}$ (mm)	−5.6	−10.9	−12.2	17.3
$\bar{\mathbf{d}}_{\text{A}}^{\text{MRI}}$ (mm)	−5.9	−12.0	−12.3	18.2
$\mathbf{d}_{\text{A}}^{\text{Sim}}$ (mm)	−3.1	−11.4	−11.2	16.3
$\mathbf{d}_{\text{A}}^{\text{Sim}} - \mathbf{d}_{\text{A}}^{\text{MRI}}$ (mm)	2.5	−0.5	1.1	1.1
Error (%)	45%	5%	9%	6%
$\mathbf{d}_{\text{A}}^{\text{Sim}} - \bar{\mathbf{d}}_{\text{A}}^{\text{MRI}}$ (mm)	2.8	0.6	1.1	1.8
Error (%)	47%	5%	9%	10%

Node B	x-axis	y-axis	z-axis	Norm
$\mathbf{d}_{\text{B}}^{\text{MRI}}$ (mm)	−2.9	−1.6	−15.6	16.0
$\bar{\mathbf{d}}_{\text{B}}^{\text{MRI}}$ (mm)	−2.1	−1.5	−14.5	14.7
$\mathbf{d}_{\text{B}}^{\text{Sim}}$ (mm)	−1.0	−5.8	−12.6	13.9
$\mathbf{d}_{\text{B}}^{\text{Sim}} - \mathbf{d}_{\text{B}}^{\text{MRI}}$ (mm)	1.9	−4.2	3.0	2.0
Error (%)	67%	254%	19%	13%
$\mathbf{d}_{\text{B}}^{\text{Sim}} - \bar{\mathbf{d}}_{\text{B}}^{\text{MRI}}$ (mm)	1.1	−4.4	1.7	0.6
Error (%)	55%	303%	12%	4%

The actual brain shift was evaluated by two indices: $\mathbf{d}_{\text{X}}^{\text{MRI}}$ and $\bar{\mathbf{d}}_{\text{X}}^{\text{MRI}}$. As shown in Table III, there is a small difference between $\mathbf{d}_{\text{X}}^{\text{MRI}}$ and $\bar{\mathbf{d}}_{\text{X}}^{\text{MRI}}$ for both regions A and B; however, they are in good agreement.

In region A, brain shifts are seen mainly in the y and z coordinates, whereas in region B, brain shift is seen mainly in the z coordinate. The gravitational force acted in the negative z-axis direction. As the brain is supported by the skull in the occipital region and by the brainstem (see Fig. 13), it is considered that the brain shifted in the negative direction of the y-axis in region A. In those coordinates (y and z coordinates in the region A, and z coordinate in region B), the proposed method estimated the brain shift reasonably well because the errors were less than 20%. A relatively large estimation error, larger than 4 (mm), was seen in the y coordinate in region B. The arachnoid trabeculae, which loosely supports the real brain, were not taken into account in the simulation. Figures 18 (a)-(c) show the comparison between the MRI-intra-brain and Sim-intra-voxel. As shown in Fig. 18, the error between the actual brain shift and simulation result is relatively large in the lower part of the brain. The errors may have occurred because the effects of the arachnoid trabeculae were not accounted for in the simulation.

D. Surface Error Analysis of the Frontal Lobe

The surface error between the MRI-intra-brain and Sim-intra-brain at the frontal lobe (around the node A) is analyzed. Impromptu regions of size $20 \geq x \geq 60$ and $-40 \geq y \geq -10$ were chosen as the ROI in the frontal lobe, because these regions were relatively flat. The nodes of the surface meshes of both MRI-intra-brain and Sim-intra-brain within the ROI were transformed into grid data using the function griddata() of MATLAB R2015b, as plotted in Fig. 19, in order to evaluate the errors along z-axis at each grid point. The errors of the Sim-intra-brain with respect to the MRI-intra-brain along z-axis at each grid (1 mm intervals) are plotted in Fig. 20.

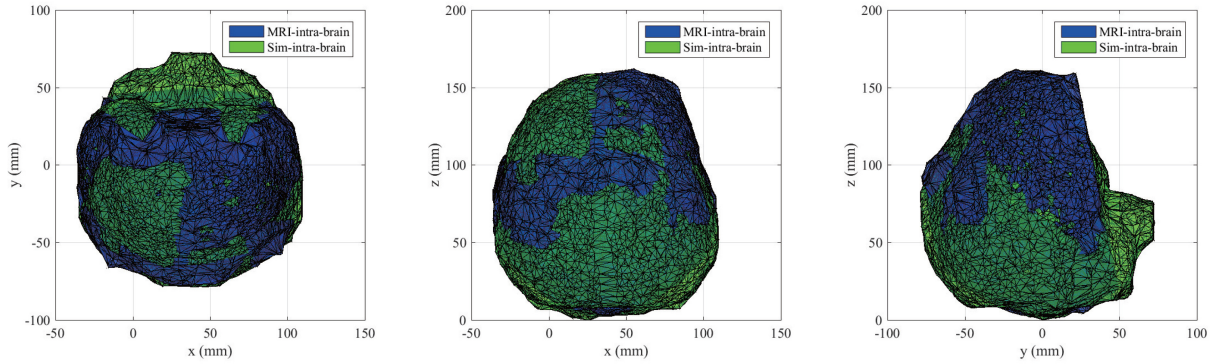

(a) x-y plane (horizontal plane) (b) x-z plane (frontal plane) (c) y-z plane (sagittal plane)

Fig. 18. The simulated brain shift (Sim-intra-brain) superimposed on the intraoperative MRI (MRI-intra-brain) in the (a) horizontal plane, (b) frontal plane, and (c) sagittal plane.

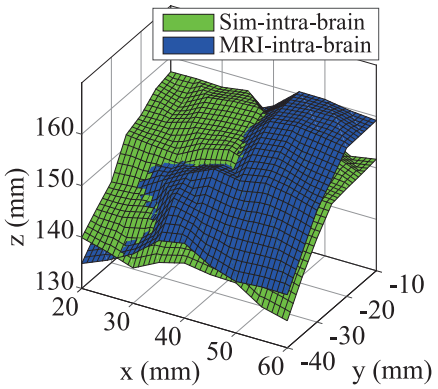

Fig. 19. Surfaces of MRI-intra-brain and Sim-intra-brain in the frontal lobe.

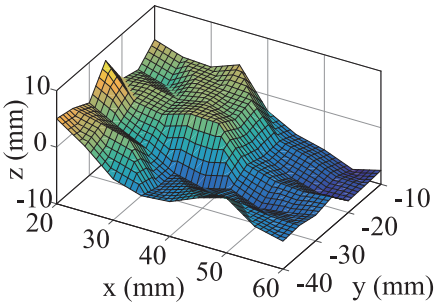

Fig. 20. Surface error of the Sim-intra-brain with respect to the MRI-intra-brain.

It is estimated that the Sim-intra-brain has errors also along x-axis and y-axis with respect to the MRI-intra-brain as shown in Table III. Therefore, the errors plotted in Fig. 20 does not signify the distance between two corresponding points. The maximum, minimum, average, and median of the distance along z-axis between the two surfaces are described in Table IV. Mean absolute error (MAE) is also described in Table IV. The average error is -2.1 mm and MAE is 3.7 mm. The maximum and minimum errors are relatively large (7.8 mm and -8.8 mm). As described in Section I, the surface error will be reduced by real-time registration using intraoperative images or point clouds.

TABLE IV
SURFACE ERROR OF THE SIM-INTRA-BRAIN WITH RESPECT TO THE MRI-INTRA-BRAIN IN THE FRONTAL LOBE

Maximum	Minimum	Average	Median	MAE
7.8 mm	-8.8 mm	-2.1 mm	-2.8 mm	3.7 mm

V. CONCLUSION

In this paper, a numerical calculation method of the brain shift caused by CSF leakage and gravity was proposed. The brain shift is estimated based on hydrostatics and FEM. As dynamic FEM was employed for the brain shift computation, the dynamic deformations can be reproduced by other researchers. In the proposed method, two kind of models are used: coarse FE model for brain shift estimation and fine surface mesh model for visualization. Each node of the surface mesh model is deformed by linearly interpolating the deformations of the neighboring nodes of the FE model. As the FE model is developed by *embedding*, the size of the FE mesh can be changed on-line considering the computational cost and accuracy.

The accuracy of the proposed method was verified by experiments using elastic gelatin cubes. The computation cost was also evaluated. When an FE model is composed of 5,000 nodes, the computation time for a simulation loop will be less than 90 (ms). Furthermore, the accuracy of the proposed method was verified through 3D models developed from the preoperative and intraoperative MRI images of a real patient. The registration between the 3D models of preoperative and intraoperative brains were done using a medical image processing software *3D Slicer*. Surface mesh models were generated from the preoperative and intraoperative brain models. Two nodes were chosen from the most anterior position of the frontal lobe and the highest position of the parietal lobe of the surface mesh preoperative brain model. The corresponding nodes were searched among the nodes of the surface mesh intraoperative brain model. Considering the distances between the nodes of the preoperative and intraoperative models as the base, the simulated brain shift was evaluated. At a node of the frontal lobe, the brain shift was estimated reasonably well because the errors were less than 3 (mm). However, in the

lower parts of the brain, the estimation errors were relatively large. At a node of the parietal lobe, the maximum error was 4.4 (mm). The effects of arachnoid trabeculae, which loosely support the real brain, were not accounted for in the simulation, and this may have caused the errors in the lower part of the brain.

Furthermore, a region of 40 mm × 30 mm in the frontal lobe was chosen as the ROI, and the surface errors at the ROI between the intraoperative MRI images and the simulated shifted brain were analyzed. The mean absolute error (MAE) between the surfaces along the z-axis (the direction of gravity) in the ROI was 3.7 mm (maximum absolute error was 8.8 mm).

The future scope of this research will be to develop a real-time intraoperative registration between the predicted model and the measured surface of organs.

REFERENCES

[1] M. L. Goodenberger and R. B. Jenkins, "Genetics of adult Glioma," *Cancer Genet.*, vol. 205, no. 12, pp. 613–621, 2012.

[2] H. Dickhaus *et al.*, "Quantification of brain shift effects by MR-imaging," in *Proc. IEEE 19th Annu. Int. Conf. IEEE Eng. Med. Biol. Soc. Magn. Milestones Emerg. Med. Eng.*, vol. 2, 1997, pp. 491–494.

[3] H.-A. Leroy, C. Tuleasca, Q. Vannod-Michel, and N. Reyns, "Intraoperative MRI guidance for right deep fronto-temporal glioma resection: How i do it," *Acta Neurochirurgica*, vol. 162, no. 12, pp. 1–5, 2020.

[4] Y. Xiao *et al.*, "Evaluation of mri to ultrasound registration methods for brain shift correction: The CuRIOUS2018 challenge," *IEEE Trans. Med. Imag.*, vol. 39, no. 3, pp. 777–786, Mar. 2020.

[5] P. Coupé, P. Hellier, X. Morandi, and C. Barillot, "3D rigid registration of intraoperative ultrasound and preoperative mr brain images based on hyperechogenic structures," *Int. J. Biomed. Imag.*, vol. 2012, Jan. 2012, Art. no. 531319.

[6] A. Ema, K. Sase, T. Tsujita, and A. Konno, "MPS-FEM coupled analysis for brain shift estimation (in Japanese)," in *Proc. Robot. Mechatron. Conf.*, 2016, pp. 1–2.

[7] E. F. Antonio, G. Stefano, and D. Daniele, "Models and tissue mimics for brain shift simulations," *Biomech. Model. Mechanobiol.*, vol. 17, no. 1, pp. 249–261, 2017.

[8] K. Sun, T. S. Pheiffer, A. L. Simpson, J. A. Weis, R. C. Thompson, and M. I. Miga, "Near real-time computer assisted surgery for brain shift correction using biomechanical models," *IEEE J. Transl. Eng. Health Med.*, vol. 2, 2014, Art. no. 2500113.

[9] K. Ebina *et al.*, "Development and validation of a measurement system for laparoscopic surgical procedures," *SICE J. Control Meas. Syst. Integr.*, vol. 13, no. 4, pp. 191–200, 2020.

[10] K. Ebina *et al.*, "Motion analysis for better understanding of psychomotor skills in laparoscopy: Objective assessment-based simulation training using animal organs," *Surg. Endoscopy*, vol. 35, no. 8, pp. 4399–4416, 2021.

[11] N. Hamzé, A. Bilger, C. Duriez, S. Cotin, and C. Essert, "Anticipation of brain shift in deep brain stimulation automatic planning," in *Proc. IEEE 37th Annu. Int. Conf. IEEE Eng. Med. Biol. Soc. (EMBC)*, 2015, pp. 3635–3638.

[12] A. Bilger, E. Bardinet, S. Fernández-Vidal, C. Duriez, P. Jannin, and S. Cotin, "Intra-operative registration for deep brain stimulation procedures based on a full physics head model," in *Proc. Workshop Deep Brain Stimul. Methodol. Challenges (MICCAI)*, 2014, pp. 1–4.

[13] T. Hartkens *et al.*, "Measurement and analysis of brain deformation during neurosurgery," *IEEE Trans. Med. Imag.*, vol. 22, no. 1, pp. 82–92, Jan. 2003.

[14] S. K. Warfield *et al.*, "Real-time registration of volumetric brain MRI by biomechanical simulation of deformation during image guided neurosurgery," *Comput. Vis. Sci.*, vol. 5, no. 1, pp. 3–11, 2002.

[15] E. Watanabe, M. Satoh, T. Konno, M. Hirai, and T. Yamaguchi, "The trans-visible navigator: A see-through neuronavigation system using augmented reality," *World Neurosurg.*, vol. 87, pp. 399–405, Mar. 2016.

[16] F. Pervin and W. W. Chen, "Mechanically similar Gel simulants for brain tissues," *Dyn. Behav. Mater.*, vol. 1, pp. 9–13, Jan. 2011.

[17] U. Chippada, *Non-Intrusive Characterization of Properties of Hydrogels*. New Brunswick, NJ, USA: Rutgers State Univ. New Jersey, 2010.

[18] "3DSlicer." [Online]. Available: https://www.slicer.org (Accessed: Mar. 10, 2020).

[19] H. Johnson, G. Harris, and K. Williams. "BRAINSFIT: Mutual information registrations of whole-brain 3D images, using the insight toolkit." Oct. 2007. [Online]. Available: https://www.insight-journal.org/browse/publication/180 (Accessed: Nov. 24, 2021).

[20] "MeshLab." [Online]. Available: http://www.meshlab.net/ (Accessed: Mar. 10, 2020).

[21] K. Sase, T. Tsujita, and A. Konno, "Embedding segmented volume in finite element mesh with topology preservation," in *Proc. Int. Conf. Med. Image Comput. Comput. Assist. Intervent. (MICCAI)*, 2016, pp. 116–123.

[22] A. C. Lui, T. Z. Polis, and N. J. Cicutti, "Densities of cerebrospinal fluid and spinal anaesthetic solutions in surgical patients at body temperature," *Can. J. Anaesthesia*, vol. 45, no. 4, p. 297, 1998.

[23] X. Chen, K. Sase, A. Konno, and T. Tsujita, "Identification of mechanical properties of brain parenchyma for brain surgery haptic simulation," in *Proc. IEEE Int. Conf. Robot. Biomimet.*, 2014, pp. 1656–1661.

[24] M. C. Murphy *et al.*, "Decreased brain stiffness in Alzheimer's disease determined by magnetic resonance elastography," *J. Magn. Reson. Imag.*, vol. 34, no. 3, pp. 494–498, 2011.

Xiaoshuai Chen received the B.E. and M.E. degrees from Tohoku University, Japan, in 2010 and 2012, respectively, and the Ph.D. degree from Hokkaido University, Japan, in 2017. In 2017, she joined Hirosaki University, where she is currently an Assistant Professor with the Faculty of Science and Technology. Her research interests include development of computer assisted surgery systems.

Ryosuke Shirai received the B.E. and M.E. degrees from Hokkaido University, Japan, in 2018 and 2020, respectively. Since 2020, he has been working with Fujitsu Lt., Japan. His research interests include development of computer assisted surgery systems.

Ken Masamune received the B.S., M.S., and Ph.D. degrees in precision machinery engineering from the University of Tokyo, Tokyo, Japan, in 1993, 1995, and 1999, respectively. From 2000 to 2005, he was a Lecturer and an Associate Professor with Tokyo Denki University, and from 2005 to 2014, he was an Associate Professor with the University of Tokyo, Graduate School of Information Science and Technology. Since 2014, he has been a Full-Time Professor with the Tokyo Women's Medical University, Faculty of Advanced Techno Surgery, Advanced Biomedical Engineering and Sciences, and a Visiting Professor with Waseda University, Joint Graduate School of Tokyo Women's Medical University and Waseda University, Cooperative Major in Advanced Biomedical Sciences. His research interests include medical robotics, mixed reality and clinical information systems in medicine, and medical device regulatory sciences. He is a Board Member of the International Society for Computer Aided Surgery, the Japan Society of Computer Aided Surgery, Society for Life Support, Robotics Society of Japan, and the Society for Nursing Science and Engineering.

Manabu Tamura received the M.D. and Ph.D. degrees from Wakayama Medical University, Wakayama, Japan, in 1995 and 2009, respectively. From 2007 to 2010, he was a Research Associate with Wakayama Medical University. From 2010 to 2017, he was a Research Associate and a Lecturer with the Institute of Advanced Biomedical Engineering and Science, Tokyo Women's Medical University, Tokyo, Japan. From 2017 to 2020, he was the Deputy Director of Bio-Industry Division, Commerce and Service Industry Policy Group, Ministry of Economy, Trade and Industry. Since 2020, he has been an Associate Professor with the Joint Graduate School of Tokyo Women's Medical University and Waseda University, Cooperative Major in Advanced Biomedical Sciences. He has been serving with the Japanese Board of Neurological Surgery.

Yoshihiro Muragaki received the M.D. degree from Kobe University in 1986, the Ph.D. degree in medical science from Tokyo Women's Medical College in 1997, and the Ph.D. degree in biomedical science from Waseda University in 2014. In 1992, he was a Certified Neurosurgeon with the Department of Neurosurgery, Tokyo Women's Medical University and an Associate Professor with the Faculty of Advanced Techno-Surgery, Tokyo Women's Medical University in 2009, where he has been a Professor since 2011. He engages in brain tumor treatment, intraoperative MRI, and regulatory science.

Kazuya Sase received the B.E. and M.E. degrees in mechanical engineering from the Tohoku University, Sendai, Japan, in 2011 and 2013, respectively, and the Ph.D. degree in system science and informatics from Hokkaido University, Sapporo, Japan, in 2017. Since 2017, he has been with Tohoku Gakuin University, Japan, where he is currently an Associate Professor with the Department of Mechanical Engineering and Intelligent Systems. His research interests include real-time physics simulation, haptic rendering, and their applications.

Teppei Tsujita (Member, IEEE) received the B.E., M.E., and Ph.D. degrees in aeronautics and space engineering from Tohoku University, Japan, in 2003, 2005, and 2009, respectively. From 2005 to 2006, he worked with the Mechanical Engineering Research Laboratory, Hitachi, Ltd., Japan. From 2008 to 2009, he was a Japan Society of the Promotion of Science Research Fellow, and from 2009 to 2015, he was an Assistant Professor with Tohoku University. He was a Visiting Faculty with the Robotics Institute, Carnegie Mellon University, USA, from 2013 to 2015. Since 2015, he has been with the National Defense Academy of Japan and currently he is an Associate Professor of Department of Mechanical Engineering. His research interests include surgical simulators, haptic devices, humanoid robots, and their applications.

Atsushi Konno (Member, IEEE) received the B.E., M.E., and Ph.D. degrees in precision engineering from Tohoku University, Sendai, Japan, in 1988, 1990, and 1993, respectively. He became a Research Associate with Tohoku University in 1993, a Research Associate with the University of Tokyo in 1995, and an Associate Professor with Tohoku University in 1998. In 2012, he was a Professor with Hokkaido University, Sapporo, Japan. His research interests include humanoid robots, unmanned aerial vehicles, surgery simulator, and their applications.